

# A measurement of cluster masses using *Planck* and SPT-SZ CMB lensing

Alexandre Huchet and Jean-Baptiste Melin

Université Paris-Saclay, CEA, Département de Physique des Particules, 91191, Gif-sur-Yvette, France.  
e-mail: alexandre.huchet@cea.fr, jean-baptiste.melin@cea.fr

Received ; accepted

## ABSTRACT

We used an unbiased CMB lensing mass estimator on 468 SPT-SZ clusters from the SPT-SZ and the *Planck* public data, the first such estimation using combined ground- and space-based data. We measured the average ratio between CMB lensing and SZ mass to be  $M_{\text{CMB lens}}/M_{\text{SZ}} = 0.98 \pm 0.19$  (stat.)  $\pm 0.03$  (syst.). The average CMB lensing mass from the combination of the two data sets is measured at  $4.8\sigma$ , which is a significant gain with respect to the measurement performed on the SPT-SZ only ( $3.9\sigma$ ) or the *Planck* only ( $3.7\sigma$ ) data set. We showed that the combination not only takes advantage of the two different ranges of spatial scales (i.e. Fourier modes) observed but also exploits the lensing induced correlation between scales observed by one experiment and the other. This result demonstrates the importance of measuring a large range of spatial scales for CMB lensing mass estimation, from arcmin to degrees. This large range of scales will most probably be provided by the combination of various data sets, such as from the large and small aperture telescopes of the upcoming Simons Observatory and future CMB-S4 experiment, and *Planck*. In this context, the *Planck* data will remain a key element for CMB lensing cluster studies in the years to come.

**Key words.** galaxies: clusters: general – cosmic background radiation – Gravitational lensing: weak – methods: statistical

## 1. Introduction

Clusters of galaxies, located at the nodes of the cosmic web, are very useful objects for studying both astrophysics and cosmology. They have played an important role in shaping and reinforcing the  $\Lambda$ CDM concordance model and have been used in many works to derive constraints on cosmological parameters (e.g., White et al. 1993; Carlberg et al. 1996; Bahcall et al. 1997; Allen et al. 2002). Among these approaches, the most promising way to constrain cosmological parameters with clusters is through cluster counts as a function of redshift and mass, which are very sensitive to cosmological parameters, particularly  $\Omega_m$  and  $\sigma_8$  (Albrecht et al. 2006; Vikhlinin et al. 2009; Allen et al. 2011). Clusters thus have the statistical power to be as efficient as other major cosmological probes but their constraints unfortunately suffer from uncertainty in the relation between cluster masses and directly observable quantities. This uncertainty on the cluster mass scale dominates current analyses (e.g., Hasefield et al. 2013; Planck Collaboration et al. 2016c; Bocquet et al. 2019; Abbott et al. 2020). However, the situation will change in the next few years with the advent of the large optical facilities *Euclid*<sup>1</sup> and the Vera Rubin Observatory<sup>2</sup>. These facilities will improve the accuracy and number of measurements of cluster masses thanks to weak gravitational lensing, up to redshifts of the order of one (Laureijs et al. 2011; LSST Science Collaboration et al. 2009). The major uncertainty for cosmology with clusters at  $z < 1$  will, therefore, be overcome in the next decade. Extending cosmological studies with clusters at redshift  $z > 1$  will not be possible with the weak gravitational lensing

on galaxies due to the lack of background sources at these redshifts. The cosmic microwave background (CMB) is hoped to be a new background source for studying the weak lensing of clusters at higher redshift. Located at  $z \sim 1100$  and having precisely known statistical properties, it makes it possible to measure masses of galaxy clusters by weak gravitational lensing in the redshift range  $0 < z < 3$ . (Zaldarriaga & Seljak 1999; Seljak & Zaldarriaga 2000; Holder & Kosowsky 2004; Dodelson 2004; Vale et al. 2004; Lewis & King 2006; Lewis & Challinor 2006).

The first tools were proposed in the mid-2000s to detect this effect (Maturi et al. 2005; Hu et al. 2007; Yoo & Zaldarriaga 2008; Yoo et al. 2010), but the first data sets for which the lensing signal became detectable only appeared in the early 2010s (Ruhl et al. 2004; Swetz et al. 2011; Planck Collaboration et al. 2020a). The signal-to-noise for CMB lensing mass measurement is very low in these data sets. Thus, it is not possible to make individual measurements and it is necessary to average the signal over several hundred clusters to pull the signal out of the noise. The first measurements were carried out almost jointly by the ACT, SPT and *Planck* collaborations shortly before the mid-2010s (Madhavacheril et al. 2015; Baxter et al. 2015; Planck Collaboration et al. 2016c). These detections were made possible thanks to the pioneering work cited above and improved tools (see Melin & Bartlett 2015). The improvement of existing tools and the development of new tools are currently active research fields (Raghunathan et al. 2017; Madhavacheril & Hill 2018; Raghunathan et al. 2019a; Horowitz et al. 2019; Patil et al. 2020; Gupta & Reichardt 2021; Levy et al. 2023; Chan et al. 2023). The motivation is to be ready to analyze data from the new generation of CMB instruments which will provide data sets that will enable individual mass measurements for the first time, the Simons Observatory (SO, Ade et al. 2019) and CMB-S4 (Abazajian et al. 2019).

<sup>1</sup> [https://www.esa.int/Science\\_Exploration/Space\\_Science/Euclid](https://www.esa.int/Science_Exploration/Space_Science/Euclid) & <https://www.euclid-ec.org>

<sup>2</sup> <https://rubinobservatory.org> & <https://lsstdesc.org>

Following its first detection in the mid-2010s, the weak gravitational lensing on the CMB has been used to measure masses of clusters selected in the optical and the infrared (Geach & Peacock 2017; Baxter et al. 2018; Raghunathan et al. 2019b; Madhavacheril et al. 2020) as well as to measure the mass of halos hosted by galaxies or quasars (Raghunathan et al. 2018; Geach et al. 2019). These measurements are performed using the intensity (i.e. temperature) maps of current data sets, but the polarized signal is expected to improve significantly the precision of the measurement in future data sets. In particular, Raghunathan et al. (2019) recently succeeded in making the first detection of the CMB cluster lensing in the SPTpol data using only the polarized signal. In parallel to these efforts, first cluster cosmological analyses using CMB cluster lensing to anchor the mass scale were performed (Planck Collaboration et al. 2016c; Zubeldia & Challinor 2019), including a careful assessment of the statistics of the recovered CMB lensing masses (Zubeldia & Challinor 2020). With the upcoming experiments (SO and CMB-S4), it will be possible to extract, from the same data set, galaxy clusters and their masses to high accuracy thanks to CMB cluster lensing, leading to competitive cosmological constraints (Louis & Alonso 2017; Madhavacheril et al. 2017; Raghunathan et al. 2022; Chaubal et al. 2022).

In this work, we used an unbiased CMB lensing mass estimator on 468 clusters from the SPT-SZ cluster catalogue (Bocquet et al. 2019). We worked on flat tangential maps cut from the all-sky *Planck* and SPT-SZ maps, and combined them. We took advantage of the different ranges of spatial scales, or Fourier modes of the maps, that the two data sets provide. The combined signal-to-noise ratio for individual mass measurement is comprised between 0.05 and 1. We thus had to average the 468 mass estimations to obtain the average mass of the whole sample.

We first introduce the two data sets used in our analysis in Sect. 2. We then explain our methodology in Sect. 3 and present our simulations in Sect. 4. We show our results in Sect. 5. We discuss uncertainties in Sect. 6. Finally, we summarize and conclude in Sect. 7.

Throughout the article, we work in the flat  $\Lambda$ CDM model with parameters  $H_0 = 70$  km/s/Mpc,  $\Omega_m = 0.3$ .

## 2. Data sets

We used two sets of sky maps in our analysis, SPT-SZ and *Planck*. Our analysis is performed on the SPT-SZ cluster catalogue only.

### 2.1. SPT-SZ sky maps

The South Pole Telescope (SPT, Ruhl et al. 2004) is a 10 m diameter mirror facility operating at the Amundsen–Scott South Pole Station in Antarctica. It observed a  $\sim 2500$  deg<sup>2</sup> area of the southern sky between 2008 and 2011, in three frequency bands centered around 95, 150 and 220 GHz, with a beam size of 1.6, 1.1 and 1.0 arcmin respectively (full width at half maximum, FWHM). This survey is referred as the SPT-SZ survey (Story et al. 2013). SZ stands for the Sunyaev-Zel’dovich effect, used to detect the clusters in this survey. The SZ effect is actually a contaminant in our study, we present it and explain how we handle it in Sec. 3.4.

We used the "SPT Only Data Maps" published by Chown et al. (2018). The maps include all three SPT-SZ frequencies, with a degraded resolution compared to the original data, that is 1.75 arcmin (FWHM) for the three maps. The SPT-SZ data con-

tain a point source mask and the transfer function of the instrument for the three frequencies. All maps are provided in equatorial coordinates, and in HEALPix format with the resolution parameter  $N_{side} = 8192$ , corresponding to a pixel size of about 0.43 arcmin. We also extracted the frequency response of each of the SPT-SZ band from Fig. 10 of Chown et al. (2018), which are useful to compute the frequency dependence of the thermal SZ effect in each frequency band  $j_{\nu_i}$  (see Sect. 3.1).

### 2.2. Planck sky maps

The *Planck* space mission (Planck Collaboration et al. 2020b) is equipped with a 1.5 m diameter telescope and two instruments, the Low Frequency Instrument (LFI) and the High Frequency Instrument (HFI). The latter observed the whole sky in six frequency bands centered at 100, 143, 217, 353, 545 and 857 GHz at a resolution of 9.659, 7.220, 4.900, 4.916, 4.675, 4.216 arcmin (FWHM) (Planck Collaboration et al. 2016a).

*Planck* HFI maps are full sky but we restrained our analysis to the SPT-SZ field in order to combine the maps.

The *Planck* maps are provided in Galactic coordinates, at a HEALPix resolution  $N_{side} = 2048$ , corresponding to a pixel size of 1.72 arcmin. To facilitate combining these maps with the SPT-SZ maps, we changed their coordinate system to equatorial, and upgraded them to  $N_{side} = 8192$  by zero-padding: we harmonic transform the maps, add zeros at high multipoles in the harmonic space, and then perform the inverse harmonic transform. We used the maps from the *Planck* Release 2 provided in the *Planck* Legacy Archive.

### 2.3. Complementarity of the two data sets

The two data sets are complementary. On the one hand, the *Planck* telescope is located in space, and its HFI mapped the sky at six different frequencies, but *Planck* has somewhat a small mirror for cluster science. On the other hand, the South Pole Telescope is ground-based, has a large mirror, a large number of detectors, but the large scales in the maps ( $> 0.5$ deg) are filtered out due to the telescope scanning strategy.

As a result, SPT-SZ has a very good resolution and sensitivity whereas *Planck* has an excellent frequency coverage and can map the large angular scales of the sky. This complementarity should bring information on correlations between large (*Planck*) and small (SPT-SZ) scales, leading to a significant improvement on the final error of our combined CMB lensing analysis compared to the analyses led on the two independent data sets.

### 2.4. SPT-SZ cluster catalogue

We used the catalogue from Bleem et al. (2015), with masses and redshifts updated by Bocquet et al. (2019). The catalogue contains 677 objects. We restricted our analysis to the 516 clusters with measured redshifts, and subsequently removed 48 clusters located close to the edge of the SPT-SZ field (see Sect. 3.2). Our final catalogue contains 468 clusters. The SPT-SZ masses  $M_{500}$  (mass enclosed in a sphere of radius  $R_{500}$  within which the average density is 500 times the critical density at the cluster’s redshift) are estimated using the SZ signal-to-noise ratio versus mass relation for a flat  $\Lambda$ CDM model ( $h = H_0/(100$  km/s/Mpc) = 0.7,  $\Omega_m=0.3$ ,  $\sigma_8 = 0.8$ ), which is calibrated from external X-ray and weak lensing data sets. The SPT-SZ masses are corrected from selection effects. We multiplied the SPT mass by a factor 0.8 to match the Arnaud et al. (2010)

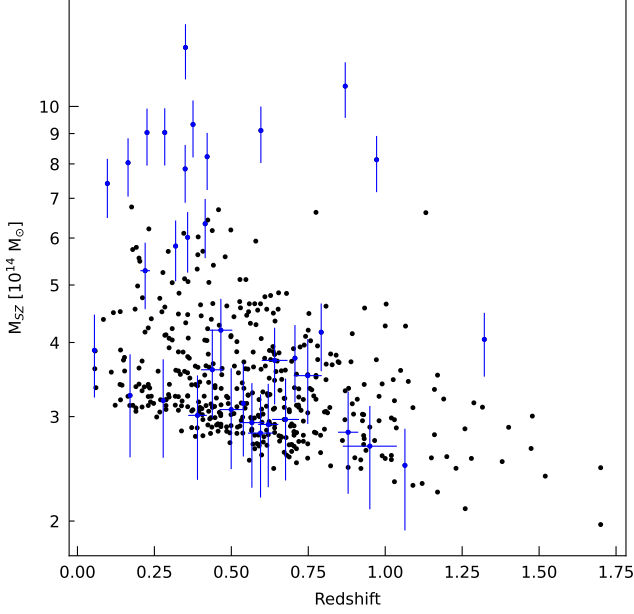


**Fig. 1.** Mass-redshift distribution of the 468 SPT-SZ clusters used in our analysis. We display in blue the error bars for the clusters with  $M_{SZ} > 7 \times 10^{14} M_{\odot}$  and of one out of 20 under this threshold for clarity.

mass definition as was done by [Tarrío et al. \(2019\)](#), [Melin et al. \(2021\)](#) and [Melin & Pratt \(2023\)](#). We denote by  $M_{SZ}$  the SPT mass rescaled by this factor 0.8. We discuss this choice in the light of our results in Sect. 7. The distribution of our sample in the mass versus redshift plane is shown in Fig. 1. Clusters span a large redshift range  $z \in [0, 1.7]$  above a mass threshold that varies slowly with redshift  $M_{SZ} \gtrsim 2 \times 10^{14} M_{\odot}$ .

### 3. Methodology

We use some of the notations from [Melin & Bartlett \(2015\)](#) in the following subsections.

#### 3.1. Concise overview

Our goal is to use an unbiased estimator to measure the mean  $M_{CMB\text{lens}}/M_{SZ}$  mass ratio. With this in mind, we did not stack the maps of all the clusters but instead built a CMB map for each cluster field, from the nine frequency maps (three SPT and six *Planck*).

We first cut tangential maps out of the nine sky maps centered at the location of each cluster. We then used an Internal Linear Combination (ILC, Sect. 3.4) to build the best lensed CMB map around the cluster. Gravitational lensing of the CMB induces correlations across its spatial scales. We used these correlations to build a lensing potential with the minimum variance estimator from [Hu & Okamoto \(2002\)](#). This lensing potential was then compared to the lensing potential of a Navarro-Frenk-White (NFW, [Navarro et al. 1996](#)) profile using a matched filter ([Melin & Bartlett 2015](#)). We can then derive the individual mass from the NFW profile. Individual errors are large (typically one to ten times larger than the signal) so we computed a weighted mean mass of the sample as our measurement.

All those steps were applied on eleven different sets of 468 locations. The first set is the one with the CMB cluster lensing

signal. We called it the *on* set. It is centered at the locations of the clusters. The ten following sets are ten draws at 468 random locations in the SPT-SZ footprint. We called them the *off* sets. We ran the same analysis on the *on* and *off* sets of maps, and subtracted at the end the average signal of the ten *off* sets from the *on* set:  $on - \langle off \rangle_{10}$ . This method allowed us to remove spurious signal from instrumental correlated noises, foreground or background astrophysical sources and any additive systematic bias. Averaging ten random sets reduces the impact on the final error, which takes the form  $\sigma = \sqrt{\sigma_{on}^2 + \sigma_{off}^2} = \sqrt{\sigma_{on}^2 (1 + \frac{1}{10})}$ .

We assumed that each field contains the primary CMB (lensed!), the thermal SZ (tSZ) signal, and noise. The noise can be of astrophysical or instrumental origin. We thus write the maps of one field in Fourier space as

$$\begin{cases} m_{\nu_0}(\mathbf{k}) = \alpha_{\nu_0}(\mathbf{k})S(\mathbf{k}) + \beta_{\nu_0}(\mathbf{k})y(\mathbf{k}) + n_{\nu_0}(\mathbf{k}) \\ m_{\nu_1}(\mathbf{k}) = \alpha_{\nu_1}(\mathbf{k})S(\mathbf{k}) + \beta_{\nu_1}(\mathbf{k})y(\mathbf{k}) + n_{\nu_1}(\mathbf{k}) \\ \dots \end{cases}, \quad (1)$$

or in a more compact way

$$\mathbf{m}(\mathbf{k}) = \boldsymbol{\alpha}(\mathbf{k})S(\mathbf{k}) + \boldsymbol{\beta}(\mathbf{k})y(\mathbf{k}) + \mathbf{n}(\mathbf{k}). \quad (2)$$

with  $S$  the primary CMB,  $y$  the tSZ Compton map of the cluster, and  $n_{\nu_i}$  the instrumental and astrophysical noises, that is all the other components in the frequency band  $\nu_i$ . We also have

$$\begin{cases} \alpha_{\nu_i}(\mathbf{k}) = b_{\nu_i}(\mathbf{k}) \times t_{\nu_i}(\mathbf{k}) \\ \beta_{\nu_i}(\mathbf{k}) = \alpha_{\nu_i}(\mathbf{k}) \times j_{\nu_i} \end{cases}, \quad (3)$$

where  $b_{\nu_i}$  and  $t_{\nu_i}$  are respectively the isotropic beam and the transfer function of the instrument in the frequency band  $\nu_i$ . This transfer function is taken as  $t_{\nu_i} = 1$  for all *Planck* frequencies but is anisotropic for SPT-SZ frequencies. Therefore,  $\alpha_{\nu_i}$  and  $\beta_{\nu_i}$  depend on the vector  $\mathbf{k}$  and not only on its modulus for SPT-SZ data, making the analysis more complex.  $j_{\nu_i}$  is the frequency dependence of the tSZ effect, integrated in the  $\nu_i$  band.

The kinetic SZ (kSZ) signal has the same frequency dependence as the primary CMB and cannot be separated from it. We estimated its impact on our result in Sect. 6.1 and corrected from it in our final measurement.

#### 3.2. Tangential maps

We performed our analysis in Fourier space from small flat tangential maps. We hence had to cut them out of the spherical HEALPix maps.

For each cluster, we cut a  $10 \times 10 \text{ deg}^2$  map centered on it, when possible. This size matches the size used for the cluster extraction in the *Planck* official analysis ([Planck Collaboration et al. 2016a](#)). It is large enough to allow for a good estimation of the covariance matrix of the maps. If the cluster was close to the border of the field of the SPT-SZ public data, that is less than 17 arcmin ( $\sim 40$  pixels), we shifted the cluster as close as possible to the center without including in the tangential maps more than 1% of bad pixels, that is empty pixels out of the SPT-SZ field. Some clusters being too close to the border, we had to remove them from our sample. We removed 48 clusters, reducing the SPT-SZ sample from 516 clusters with redshift to 468 clusters with redshift and well within the SPT-SZ public field. The SPT transfer function is not azimuthally symmetric. We estimated it as in [Melin et al. \(2021\)](#). We computed it, for each

frequency, at the location of the 468 SPT clusters under the form of an HEALPix map. We then cut  $10 \times 10 \text{ deg}^2$  maps around the cluster location, averaged them and symmetrised over the horizontal and vertical directions to obtain a single transfer function per frequency. Throughout the analysis, we apodised the maps in real space to avoid artifacts when using the (2-dimensional) Fourier transform.

### 3.3. Point sources handling

The tangential maps contained point sources that we needed to remove to avoid contamination of our lensing estimator. To do so, we replaced a circular zone slightly larger than the FWHM of the beam centered at the point source location by a constrained Gaussian realisation. This filling had to be continuous with the surrounding data in order to reduce the impact on our lensing estimator.

For each cluster, we had 9 maps – 6 *Planck* and 3 SPT-SZ – that we masked separately. We first computed the signal-to-noise ratio of the point sources in each map using a single frequency matched filter. We then iterated on the sources verifying  $S/N > 6$  and masked them with a disk of radius  $r_i$  of 3 (resp. 10) arcmin for SPT-SZ (resp. *Planck*).

To mask the point sources, we could not simply set the masked regions to zero, no matter how smooth their edges were. We later measured correlations between different k-modes (spatial scales) of the map, and these masked regions would only have created fake correlations if filled with zeros. To ensure that we were not creating artificial correlations, we used the [Hoffman & Ribak \(1991\)](#) constrained Gaussian field method (see also [Benoit-Lévy et al. 2013](#)).

We first computed a random realisation of a Gaussian temperature field  $\tilde{m}$  from the 2-dimensional power spectrum  $P(\mathbf{k})$  of the map to be masked  $m$ . This random realisation was expected to fill the hole and, although it already had the same variance as  $m$ , it needed to be continuous with the neighbouring original map pixels. We thus had to constrain it, using an annulus encircling the masked zone named the calibrating zone. We chose it with an outer radius  $r_o$  of twice the inner radius  $r_i$ , the radius of the masked zone. We illustrate the disk and annulus in Fig. 2.

We now had a zone to mask with a field  $m_1$  and a constraining zone with a field  $m_2$  in the original map, and the same for the Gaussian realisation ( $\tilde{m}_1$  and  $\tilde{m}_2$ ).

The second step involved computing the 2-dimensional correlation function of  $m$ , that we noted  $\xi(\mathbf{r})$  with  $\mathbf{r}$  the distance between two pixels.  $\xi(\mathbf{r})$  is the inverse Fourier transform of  $P(\mathbf{k})$ , and describes the most likely value of a pixel given the values of other pixels at different distances. From this function, we can obtain the covariance matrix for chosen sets of pixels. We created two of them, one being the auto-covariance matrix of the constraining zone  $\Sigma_{22}$  and the other one the covariance matrix between the masked zone and the constraining one  $\Sigma_{12}$ . We understand now why we used the correlation function on the whole map to compute those, as number of pixels in the constraining zone might not be enough to compute  $\Sigma_{22}$  accurately and, since the values of  $m_1$  are the ones we have to get rid of, we cannot use only them to compute  $\Sigma_{12}$ .

The conditional probability distribution function of a field  $m'_1$  constrained by  $m'_2$  is

$$\mathcal{P}(m'_1|m'_2) = \frac{\mathcal{P}(m'_2|m'_1)\mathcal{P}(m'_1)}{\mathcal{P}(m'_2)}, \quad (4)$$

and it is a Gaussian centered on

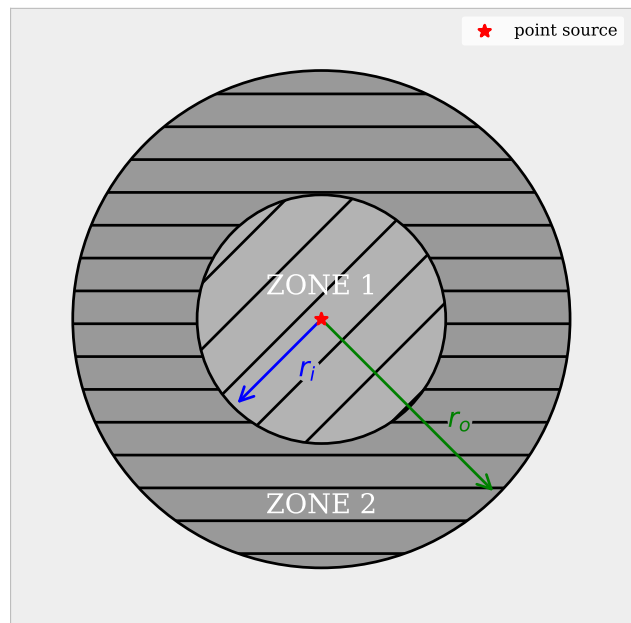


**Fig. 2.** Diagram of the two zones used for in-painting. Zone 1 is the in-painted area (the masked zone), and zone 2 is the area constraining our Gaussian field to ensure continuity (the constraining zone). The inner radius  $r_i$  is 3 (resp. 10) arcmin for SPT (resp. *Planck*) and the outer radius  $r_o$  is twice the inner one.

$$\bar{m}'_1 = \langle \mathcal{P}(m'_1|m'_2) \rangle = \Sigma_{12}\Sigma_{22}^{-1}m'_2. \quad (5)$$

$\bar{m}'_1$  can be seen as the most probable value for each pixel in zone 1 *individually*, i.e. what we should get if we know  $m'_2$  and  $\xi(\mathbf{r})$ . This does not mean that  $\bar{m}'_1$  had the same statistical properties as the CMB we wanted to reconstruct: it lacked the deviations between the values in zone 1 inferred from zone 2 only and the actual values. These deviations that describe the large scales that we cannot constrain from zone 2 were obtained from the simulation.

Our field  $\tilde{m}_1$  already contained the appropriate random variations because we built it with  $P(\mathbf{k})$ , but it needed to be offset to have the same mean as  $m_1$  should have.

The third step was to compute the residual of the realisation, defined as

$$m_{1,r} = \tilde{m}_1 - \bar{\tilde{m}}_1 = \tilde{m}_1 - \Sigma_{12}\Sigma_{22}^{-1}\tilde{m}_2, \quad (6)$$

which is the field with only the random variations from the most probable zone 1,  $\bar{\tilde{m}}_1$  (induced from the correlations with zone 2).

The last step was then to add  $\bar{m}_1$ , that is the mean  $m_1$  should have:

$$m_{1,fill} = m_{1,r} + \bar{m}_1 = \tilde{m}_1 + \Sigma_{12}\Sigma_{22}^{-1}(m_2 - \tilde{m}_2). \quad (7)$$

$m_{1,fill}$  is used to fill the zone to mask, it is continuous with the surrounding pixels and has the expected standard deviation.

### 3.4. Internal linear combination

We had nine point-source-free maps for each cluster, but they were still contaminated by the tSZ effect ([Carlstrom et al. 2002](#)). The maps were written in column in the form of Eq. 2.

We clearly see where our signal lies and we look for a minimum variance estimate  $\hat{S}$  of the pure lensed CMB map  $S$ . We used the method provided by [Remazeilles et al. \(2011\)](#), called constrained Internal Linear Combinations (ILC) to obtain our minimum variance estimate while nulling the tSZ signal. As its name suggests, its aim is to recover the signal thanks to a linear combination of the frequency maps, i.e.

$$\hat{S} = \mathbf{w}^t \mathbf{m}. \quad (8)$$

A derivation of the constraints  $\mathbf{w}^t \boldsymbol{\alpha} = 1$  and  $\mathbf{w}^t \boldsymbol{\beta} = 0$  gives

$$\mathbf{w}^t = \frac{(\boldsymbol{\beta}^t \hat{\mathbf{R}}^{-1} \boldsymbol{\beta}) \boldsymbol{\alpha}^t \hat{\mathbf{R}}^{-1} - (\boldsymbol{\alpha}^t \hat{\mathbf{R}}^{-1} \boldsymbol{\beta}) \boldsymbol{\beta}^t \hat{\mathbf{R}}^{-1}}{(\boldsymbol{\alpha}^t \hat{\mathbf{R}}^{-1} \boldsymbol{\alpha}) (\boldsymbol{\beta}^t \hat{\mathbf{R}}^{-1} \boldsymbol{\beta}) - (\boldsymbol{\alpha}^t \hat{\mathbf{R}}^{-1} \boldsymbol{\beta})^2}, \quad (9)$$

where  $\hat{\mathbf{R}}$  is the empirical covariance matrix of the nine maps. In their work, [Remazeilles et al. \(2011\)](#) compute  $\hat{\mathbf{R}}$  with an average on  $l$ -intervals in spherical harmonics in order to limit the statistical variations. In our case, because the SPT transfer function is strongly anisotropic, we could not use the same method. We computed  $\hat{\mathbf{R}}$  on all the *on* and *off* fields and performed the average on individual  $\mathbf{k}$  modes to preserve the maximum of information. We averaged indiscriminately the *on* and *off* maps because the CMB lensing signal is not expected to affect the ILC reconstruction of the CMB when averaged over all the maps.

This method allowed us to recover the best CMB from the nine frequency maps, but the noise at small scales was very large in the final map due to the deconvolution of the beams and transfer functions  $\boldsymbol{\alpha}$  and  $\boldsymbol{\beta}$ . We thus applied an effective beam  $\tilde{b}$  to the map that flattened the noise at small scales. This effective beam was taken into account in the lensing estimator in Sect. 3.5. For the *Planck* only analysis, we used a Gaussian beam with a FWHM of 4.9 arcmin, whereas for the SPT-SZ only analysis we used the value of  $\alpha_{\nu_i}(k)$  that had the smallest modulus mode-wise out of the three frequencies. For the joint analysis, the effective beam was taken as the largest modulus mode-wise between the *Planck* effective beam and the SPT-SZ effective beam in Fourier space.

The mean power spectrum of the final map convolved by the effective beam is:

$$P_{\hat{S}} = \langle |\tilde{b} \mathbf{w}^t \mathbf{m}|^2 \rangle = |\tilde{b}|^2 \frac{(\boldsymbol{\beta}^t \hat{\mathbf{R}}^{-1} \boldsymbol{\beta})^2 (\boldsymbol{\alpha}^t \hat{\mathbf{R}}^{-1} \boldsymbol{\alpha}) - (\boldsymbol{\alpha}^t \hat{\mathbf{R}}^{-1} \boldsymbol{\beta})^2 (\boldsymbol{\beta}^t \hat{\mathbf{R}}^{-1} \boldsymbol{\beta})}{\left[ (\boldsymbol{\alpha}^t \hat{\mathbf{R}}^{-1} \boldsymbol{\alpha}) (\boldsymbol{\beta}^t \hat{\mathbf{R}}^{-1} \boldsymbol{\beta}) - (\boldsymbol{\alpha}^t \hat{\mathbf{R}}^{-1} \boldsymbol{\beta})^2 \right]^2}, \quad (10)$$

where  $\langle \rangle$  is the ensemble average over various hypothetical sky realisations.  $P_{\hat{S}}$  is used in the definition of the lensing potential operator in the next section.

This method was used on the maps of the nine frequencies for  $|\mathbf{k}| < 175$  (or equivalently  $l < 6287$ ), i.e. when still in the original *Planck* resolution. For  $175 \leq |\mathbf{k}| < 278$ , where *Planck* does not provide information, we only used the three maps from SPT. At  $|\mathbf{k}| \geq 278$ , equivalent to  $l > 10000$ , neither SPT nor *Planck* provide any reliable information, we thus masked the corresponding ILC  $\mathbf{k}$  modes.

### 3.5. Lensing potential estimation

We then had to recover the lensing signal from the pure lensed CMB map obtained in the previous section. This signal is linked

to the gravitational potential, directly related to the mass projected along the line of sight, and can therefore be used to measure the mass of the cluster. We chose the [Hu & Okamoto \(2002\)](#) minimum variance lensing estimator to do so. This estimator uses the fact that the CMB lensing induces correlations between the CMB  $\mathbf{k}$  modes. They define the estimator in spherical harmonics but we used the flat-sky equivalent, as done in [Melin & Bartlett \(2015\)](#). The deflection (or lensing) potential  $\hat{\phi}$  was computed in Fourier space as follows:

$$\hat{\phi}(\mathbf{K}) = A(\mathbf{K}) \sum_{\mathbf{k}} \hat{S}^*(\mathbf{k}) \hat{S}(\mathbf{k}') F(\mathbf{k}, \mathbf{k}'), \quad (11)$$

where  $\mathbf{K} \equiv \mathbf{k} - \mathbf{k}' \pmod{n}$ , with  $n$  the size of the image in pixels along the x or y axis. The normalisation  $A$ , that is also the variance of the reconstructed lensing potential, is defined as

$$A(\mathbf{K}) = \left[ \sum_{\mathbf{k}} f(\mathbf{k}, \mathbf{k}') F(\mathbf{k}, \mathbf{k}') \right]^{-1}, \quad (12)$$

with the weights  $F$  defined to minimise the variance of the estimator  $\hat{\phi}$ :

$$F(\mathbf{k}, \mathbf{k}') = \frac{f^*(\mathbf{k}, \mathbf{k}')}{2P_{\hat{S}}(\mathbf{k})P_{\hat{S}}(\mathbf{k}')}, \quad (13)$$

$P_{\hat{S}}$  being the mean of the ILC power spectrum defined in Eq. 10. The minimum variance filter  $f$  is defined as:

$$f(\mathbf{k}, \mathbf{k}') = \tilde{b}^*(\mathbf{k}) \tilde{b}(\mathbf{k}') \left[ \tilde{C}_{\mathbf{k}} \mathbf{k} \cdot \mathbf{K} - \tilde{C}_{\mathbf{k}'} \mathbf{k}' \cdot \mathbf{K} \right], \quad (14)$$

with  $\tilde{b}$  the effective instrumental beam applied to the combination of the nine maps (Sect. 3.4).  $\tilde{C}_{\mathbf{k}}$  is the power spectrum of the unlensed CMB. We obtained it from an all-sky pure CMB Gaussian simulation at HEALPix resolution  $N_{\text{side}} = 8192$ , drawn from the *Planck* primary CMB power spectrum, that we projected and apodised as we did for the sky maps (Sect. 3.2).

### 3.6. Matched filter

We then wanted to measure a mass from the reconstructed lensing profile. To this end, we used the matched filter described in [Melin & Bartlett \(2015\)](#):

$$M_{\text{CMB lens}}/M_{\text{fiducial}} = \left[ \sum_{\mathbf{K}} \frac{|\Phi(\mathbf{K})|^2}{A(\mathbf{K})} \right]^{-1} \sum_{\mathbf{K}} \frac{\Phi^*(\mathbf{K})}{A(\mathbf{K})} \hat{\phi}(\mathbf{K}), \quad (15)$$

where  $\Phi$  is the lensing potential of a Navarro-Frenk-White (NFW) density profile (see [Navarro et al. 1996](#)) for a given fiducial cluster mass  $M_{\text{fiducial}}$ . We detailed this profile and its use in Sect. 4.1.

The matched filter returns the amplitude of our mass measurement with respect to the chosen fiducial mass and can, because of a low S/N, return a negative amplitude and as a consequence a negative mass. Because the individual error bars were large, we averaged the individual measurement over the full sample of 468 clusters. Performing individual measurements also allowed us to check for redshift and mass dependence of our  $M_{\text{CMB lens}}/M_{\text{fiducial}}$ .

## 4. Simulations

We first tested the method on simulated data to study the statistics of the recovered mass and assess for possible biases. Therefore, we built nine lensed CMB maps for each cluster, with the instrumental characteristics of the nine frequencies.

### 4.1. Cluster deflection potential

We chose a NFW density profile (Navarro et al. (1996)) for the cluster,

$$\rho(r) = \frac{\delta_c \rho_c}{(r/r_s)(1+r/r_s)^2}, \quad (16)$$

where  $\rho_c$  is the critical density at redshift  $z$  and  $r_s = R_{500}/c_{500}$  the scale radius, with  $R_{500}$  the radius inside which the cluster density is 500 times  $\rho_c$ .  $c_{500}$  is the concentration parameter that we assumed to be constant  $c_{500} = 3$  for simplicity, although it is expected to weakly vary with the mass and redshift of the cluster (e.g. Diemer & Kravtsov 2015; Ludlow et al. 2016). The characteristic overdensity  $\delta_c$  is linked to  $c_{500}$  as follows:

$$\delta_c = \frac{500}{3} \frac{c_{500}^3}{\ln(1+c_{500}) - c_{500}/(1+c_{500})}. \quad (17)$$

We projected this density profile along the line of sight up to a distance of  $5R_{500}$  from the center of the cluster and obtained a surface density profile

$$\Sigma_{NFW}(r_\perp) = \int_{los} \rho(r_\perp, l) dl. \quad (18)$$

We followed Bartelmann & Schneider (2001) to obtain the lensing profile from the surface mass density of the cluster. We first got the convergence

$$\kappa(\theta) = \frac{\Sigma_{NFW}(D_d\theta)}{\Sigma_{crit}}, \quad \text{where } \Sigma_{crit} = \frac{c^2}{4\pi G} \frac{D_s}{D_d D_{ds}}, \quad (19)$$

with  $\theta$  the angular distance to the center of the cluster.  $\Sigma_{crit}$  is the critical surface mass density above which the lensing produces multiple images, i.e. it separates weak and strong lensing.  $D_d$ ,  $D_s$  and  $D_{ds}$ , are respectively the distances observer-lens (i.e. observer-cluster), observer-source (i.e. observer-CMB) and lens-source (i.e. cluster-CMB).

From the convergence  $\kappa$ , we derived the lensing potential

$$\Phi(\theta) = \frac{1}{\pi} \int_{\mathbb{R}^2} \kappa(\theta') \ln|\theta - \theta'| d^2\theta'. \quad (20)$$

This potential was used in the simulation of the lensed CMB maps, but also in the matched filter from Eq. 15. It does not depend on the observed frequency. We used it for building the lensed maps.

### 4.2. Thermal SZ distortion

We also needed to model the thermal SZ signal from the cluster. This signal is proportional to the electron pressure of the intracluster gas (Carlstrom et al. 2002). We used the approach of Nagai et al. (2007) and Arnaud et al. (2010), with a generalized NFW electron pressure profile (gNFW):

$$P(r) = \frac{P_{500} P_0}{(r/r_s)^\gamma [1 + (r/r_s)^\alpha]^{(\beta-\gamma)/\alpha}}, \quad (21)$$

where  $(\gamma, \alpha, \beta)$  are the slope of the profile at distances  $r \ll r_s$ ,  $r \sim r_s$  and  $r \gg r_s$  respectively.  $P_0$  is the normalisation and  $P_{500} \propto M_{500}^{5/3}$  is a characteristic pressure with  $M_{500}$  the cluster mass inside  $R_{500}$ . The SZ signal is used to detect clusters and to estimate masses in combination with external data (Bocquet et al. 2019). We used these  $M_{SZ}$  masses (rescaled with a factor 0.8 as discussed in Sect. 2.4) as the fiducial mass  $M_{fiducial}$  to simulate our clusters (dark matter NFW, tSZ) and build the lensing profile for the matched filter.

We used the Arnaud et al. (2010) values for the parameters in Eq. 21 and derived the Compton parameter  $y$ :

$$y(\theta) = \frac{\sigma_T}{m_e c^2} \int_{los} P(D_d\theta, l) dl, \quad (22)$$

with  $\sigma_T$  the Thomson cross-section and  $m_e c^2$  the electron rest mass energy.

The SZ temperature distortion  $\Delta T_{SZE}$  at a frequency  $\nu$  and a distance  $r$  from the center of the cluster is then given by

$$\frac{\Delta T_{SZE}}{T_{CMB}}(\nu, \theta) = j_\nu y(\theta), \quad (23)$$

where we see the separated dependence of the tSZ effect in position  $\theta$  and frequency  $\nu$ . We included relativistic corrections to  $j_\nu$  following Sect. 3.3 of Melin & Pratt (2023). We used the cluster mass-temperature from Eq. 19 of Bulbul et al. (2019) for each cluster and the formula of Itoh et al. (1998). The tSZ spectrum including the relativistic correction was integrated over the spectral bandwidth of each of the nine frequency bands.

### 4.3. Final maps

For each frequency map, we put the same realisation of CMB  $\tilde{S}$ , generated from the CMB power spectrum provided by Planck Collaboration et al. (2016b). We then used the cluster deflection potential to obtain the lensed CMB  $S$  (Bartelmann & Schneider 2001).

$$S = \tilde{S} + \nabla \tilde{S} \cdot \nabla \Phi. \quad (24)$$

This lensed CMB, common between all frequencies was then altered with frequency or instrumental dependant elements. We added the SZ effect  $\Delta T_{SZE}$  in the maps and convolved them with the corresponding beam, before adding the appropriate noise, the same way we defined the maps in Eq. 1. For the simulations, we assumed that the instrumental noise is white with levels of 40, 18 and 70  $\mu\text{K.arcmin}$  at 95, 150 and 220 GHz for SPT-SZ, and 38, 31, 46,  $1.4 \times 10^2$ ,  $1.3 \times 10^3$ ,  $5.5 \times 10^4$   $\mu\text{K.arcmin}$  at 100, 143, 217, 353, 545 and 857 GHz for Planck.

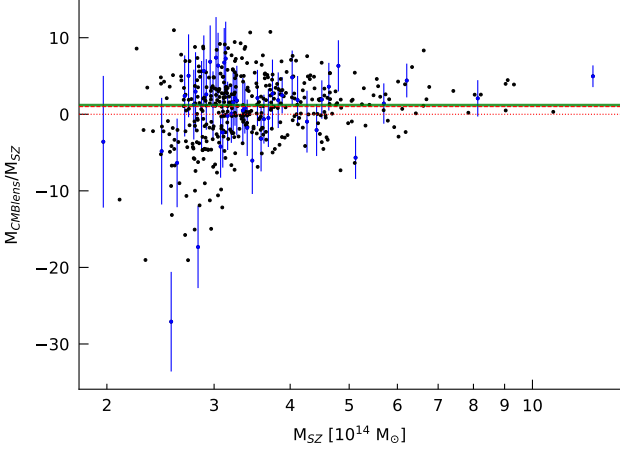


**Fig. 3.** Recovered CMB lensing mass  $M_{\text{CMBlens}}$  (divided by the input fiducial mass  $M_{\text{SZ}}$ ) as a function of the input fiducial mass for the joint *Planck* and SPT-SZ analysis of non periodic simulations. Black dots are individual measurements. Error bars are shown in blue but we display only one out of ten for clarity. The dotted (resp. dashed) red line is the zero (resp. unity) level. The green stripe is the weighted mean  $\langle M_{\text{CMBlens}}/M_{\text{SZ}} \rangle = 1.19 \pm 0.18$ .

#### 4.4. Results on simulations

For each of our 468 SPT-SZ clusters, we simulated nine frequency maps with the cluster CMB lensing signal ( $\Phi$  and  $\Delta T_{\text{CMB}}$ ), the *on* maps. We also simulated ten sets of nine frequency maps without the CMB lensing signal as the *off* maps. By doing  $on - \langle off \rangle_{10}$ , we removed spurious signal from instrumental correlated noises, foreground or background astrophysical sources and any additive systematic bias. In the simulations, we first created periodic maps, that is where the edges have continuity with the opposite one. We did not apodise the periodic maps. We also placed clusters at the center of the maps to avoid any systematic effect linked to non periodicity. In this scenario, we found no bias in our measurement, and we did not need to remove the average of the *off* maps to estimate the masses. It shows that the method itself does not suffer from any bias when the true lensing profile is known and when the maps do not contain any correlated noise, or foreground/background sources.

This case, however, is not fully realistic. Some of our clusters were not centered in the maps and the CMB is certainly not continuous from one edge to the opposite one. If a cluster is not centered, it has a non periodic lensing signal. Since it would otherwise cause problems when performing Fourier transforms, we still put a periodic signal centered on the cluster position in the matched filter and we used the *off* maps to correct the bias it incurs. In order to create non periodic maps with reduced correlation between their edges, we created simulated maps five times larger than the final size, and we kept only the central part.

Results for the joint *Planck* and SPT-SZ analysis are shown in Fig. 3 and last line of Table 1. Individual measurements are shown as black dots and have large errors bars ( $S/N \sim 0.1 - 1$ ) in blue. Averaging over the full sample provides  $\langle M_{\text{CMBlens}}/M_{\text{SZ}} \rangle = 1.19 \pm 0.18$  (green stripe) compatible with one as expected.

In Table 1, we also show the result for *Planck* only and SPT-SZ only simulations in line one and two. Both results are compatible with one as expected. More importantly, the *Planck* only error is  $\sigma_{\text{Planck}} = 0.27$ , while the SPT-SZ only error is

**Table 1.** Results on simulations, for a single realisation of a SPT-SZ-like catalogue.

Data sets	$M_{\text{CMBlens}}/M_{\text{SZ}}$
<i>Planck</i>	$1.42 \pm 0.27$
SPT-SZ	$1.17 \pm 0.25$
<i>Planck</i> + SPT-SZ	$1.19 \pm 0.18$

$\sigma_{\text{SPT}} = 0.25$ , close to the *Planck* error. The joint analysis provides an error  $\sigma = 0.19 \sim \sqrt{\frac{1}{1/\sigma_{\text{Planck}}^2 + 1/\sigma_{\text{SPT}}^2}}$  showing that there is indeed some additional information to gain in combining the two data sets. We investigated further the complementarity of the two data sets in Sect. 5.

These runs on simulation demonstrate that our pipeline is able to extract the average CMB lensing mass of the cluster sample, and provides a joint error which is a factor of  $\sim \sqrt{2}$  better than the error bar of individual experiments. We also made use of these simulations to assess the impact of modeling uncertainties on our results in Sect. 6.

## 5. Results

We first present the cluster mass measurements from *Planck* and SPT-SZ data separately in Sect. 5.1. We then show the measurement from the joint analysis in Sect. 5.2 and discuss the improvement with respect to individual analyses.

### 5.1. Masses from individual data sets

The pipeline was first used to measure the masses of the 468 clusters with the *Planck* and SPT-SZ data sets separately in order to quantify the gain due to the combination of both.

#### 5.1.1. CMB lensing masses from *Planck* only

The result for the *Planck* only data set is shown in Fig. 4. Black dots are individual measurements, and individual error bars are shown in blue for one measurement out of ten for clarity. The weighted mean of our measurement is  $M_{\text{CMBlens}}/M_{\text{SZ}} = 1.03 \pm 0.27$ . This is a  $3.7 \sigma$  measurement. It is consistent with unity, showing that the *Planck* CMB lensing mass measurement is compatible with the SZ mass measurement  $M_{\text{SZ}}$ , that is the SPT-SZ mass measurement multiplied by 0.8. The error bars we obtained are similar to the ones of the simulations, hinting that the *Planck* maps are well modelled in the simulations.

#### 5.1.2. CMB lensing masses from SPT-SZ only

The result for the SPT-SZ only data set is shown in Fig. 5. We measured an average ratio  $M_{\text{CMBlens}}/M_{\text{SZ}} = 1.12 \pm 0.29$ , a  $3.9 \sigma$  measurement. It is in agreement with the *Planck* only measurement and the SZ mass  $M_{\text{SZ}}$ . In this case, the error bars are somewhat larger than on the simulations. This is probably due to the fact that the noise in the data is more complex than the assumption of simple white noise in the simulations.

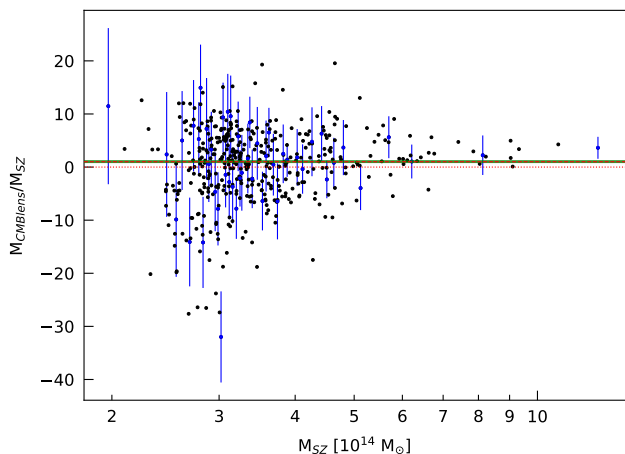


**Fig. 4.** Recovered CMB lensing mass  $M_{\text{CMBlens}}$  (divided by the SZ mass  $M_{\text{SZ}}$ ) as a function of the SZ mass for the *Planck* only analysis. Black dots are individual measurements. Error bars are shown in blue but we display only one out of ten for clarity. The dotted (resp. dashed) red line is the zero (resp. unity) level. The green stripe is the weighted mean  $\langle M_{\text{CMBlensing}}/M_{\text{SZ}} \rangle = 1.03 \pm 0.27$ .

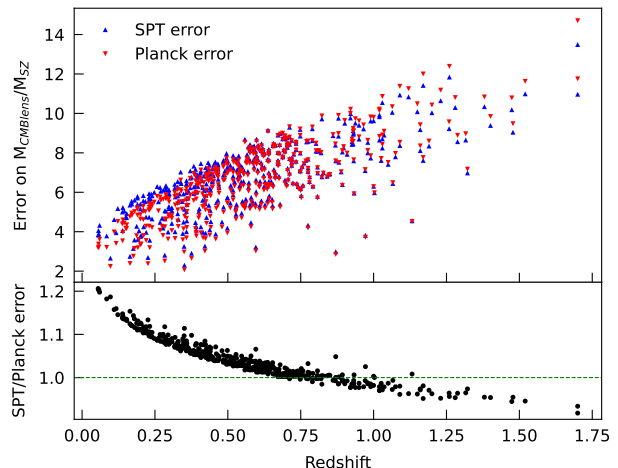


**Fig. 6.** Comparison of the errors on the SPT and *Planck* masses as a function of redshift  $z$ . The top panel displays the errors while the bottom panel displays the ratio of the errors. There is a clear correlation between the ratio of the errors due to the redshift dependence of the lensing potential  $\Phi$ .

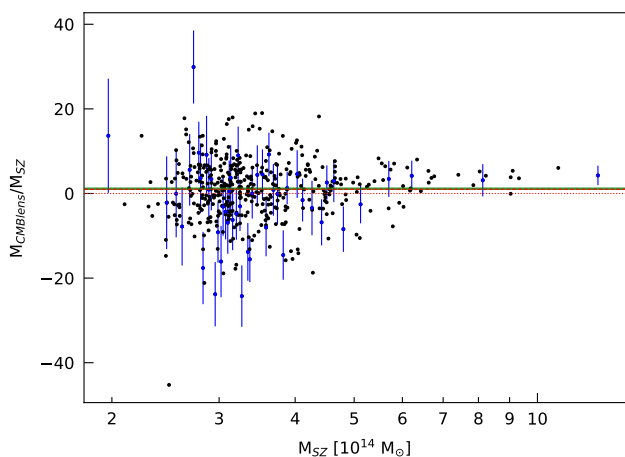


**Fig. 5.** Recovered CMB lensing mass  $M_{\text{CMBlens}}$  (divided by the SZ mass  $M_{\text{SZ}}$ ) as a function of the SZ mass for the SPT-SZ only analysis. Black dots are individual measurements. Error bars are shown in blue but we display only one out of ten for clarity. The dotted (resp. dashed) red line is the zero (resp. unity) level. The green stripe is the weighted mean  $\langle M_{\text{CMBlensing}}/M_{\text{SZ}} \rangle = 1.12 \pm 0.29$ .

### 5.1.3. Comparison of *Planck* and SPT-SZ individual error bars

We now compare individual error bars from the *Planck* only and the SPT-SZ only measurements. Fig. 6 (top panel) shows the SPT-SZ and the *Planck* error bars as a function of redshift. The bottom panel shows the ratio of the two. *Planck* provides error bars smaller than SPT-SZ at  $z < 1$ , while SPT-SZ is more efficient than *Planck* at  $z > 1$ . However the ratio between the two remains close to unity with a factor around 1.2 at maximum (reached for the lowest redshift clusters). We note the strong correlation between the two errors bars as a function of redshift. Error bars are given by the expression  $\left[ \sum_K \frac{|\Phi(\mathbf{K})|^2}{A(\mathbf{K})} \right]^{-1/2}$  with  $A(\mathbf{K})$ , the variance of the Hu & Okamoto estimator, being independent

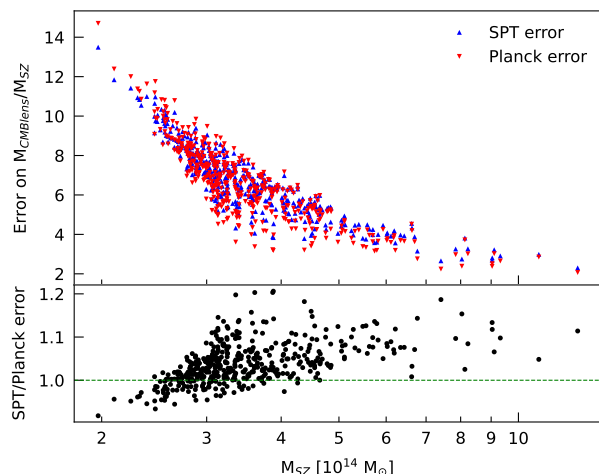


**Fig. 7.** Comparison of the errors on the SPT and *Planck* masses as a function of the SZ mass  $M_{\text{SZ}}$ . The top panel displays the errors while the bottom panel displays the ratio.

of the cluster properties (mass or redshift). Thus, at fixed mass, the redshift dependence is given by the redshift dependence of the potential  $\Phi$  (or equivalently  $\kappa$ ). So the redshift dependence of the ratio of the two errors is driven by the angular diameter distance  $D_d$  in  $\Sigma_{\text{NFW}}(D_d\theta)$ .

Fig. 7 shows the SPT-SZ and the *Planck* error bars as a function of mass, and the corresponding ratio. *Planck* outperforms SPT-SZ at high mass ( $M_{\text{SZ}} > 3 \times 10^{14} M_{\odot}$ ) while SPT-SZ is more efficient at the low mass end. The dispersion of error bar ratios with respect to mass exceeds that observed for redshift dependence. This dispersion is driven by the redshift distribution of clusters at a given mass.

## 5.2. Joint extraction of cluster masses

For the *Planck* and SPT-SZ combined analysis on the 468 clusters, we obtained a global average ratio  $M_{\text{CMBlens}}/M_{\text{SZ}} = 0.92 \pm 0.19$ , that is a  $4.8 \sigma$  measurement of the lensing signal. As expected, the joint measurement is also in agreement with the SZ mass  $M_{\text{SZ}}$ . The individual measurements are shown in Fig. 8. We averaged them in five equally logarithmically spaced mass bins (red dots and associated error bars). The global average ratio is shown as a green stripe. The red dots present a small increasing trend with mass. We show the pull of the measurements in Fig. 9, as a function of redshift (left) and mass (right). The pull is close to a normal distribution. However, in the right panel, one can see the same mass trend as in Fig. 8. This trend may be a hint that the  $M_{\text{SZ}}$  masses are overestimated at low mass and underestimated at high mass, or that there is a residual systematic bias in our measurement as a function of mass. The pull as a function of redshift (left panel) does not show any trend.

The global improvement from individual ( $3.7$  and  $3.9\sigma$ ) to the joint ( $4.8\sigma$ ) measurement is clear. In Fig. 10, we aim at comparing the errors from *Planck* only, SPT-SZ only and *Planck*+SPT-SZ as a function of the spatial scale  $K$  (or equivalently  $L$ ).  $A_i(K)$  is the variance of the error on the estimated lensing potential  $\hat{\phi}(K)$  for the considered experiment  $i$  ( $i$  standing for SPT or *Planck*). The ratio  $A_{\text{SPT+Planck}}(K)/A_i(K)$  thus compares the variance of the error of the joint measurement to the variance of the error from an individual data set measurement (SPT or *Planck*). This ratio is lower than unity for SPT and *Planck* (blue and red triangles), showing that the joint analysis provides a better measurement than individual analyses at all scales  $K$ . The *Planck* dataset brings most of the information at large scales ( $K < 50.9$  or  $L < 1830$ ), as expected, while the SPT-SZ dataset provides information at small scales ( $K > 145.0$  or  $L > 5208$ ). The ranges of scales observed by SPT-SZ and *Planck* overlap but are not identical. We also computed the sum  $A_{\text{SPT+Planck}}(K)/A_{\text{SPT}}(K) + A_{\text{SPT+Planck}}(K)/A_{\text{Planck}}(K)$  (black points). It is expected to be equal to unity if the two measurements of  $\hat{\phi}(K)$  from SPT and *Planck* are independent, that is the inverse variance of the combination is the sum of the inverse variance of individual measurements. This is the case for  $K = 18.9$  ( $L = 680$ ). For  $K < 18.9$  the sum exceeds unity showing that there is redundant information in SPT-SZ and *Planck* data. However, the combined analysis still provides a better measurement than SPT-SZ or *Planck* only for these modes as already noticed. More interestingly, the sum reaches values significantly below unity for  $K > 18.9$ , showing that the combination provides a better measurement than independent measurements: the combination takes advantage of correlations between scales  $k$  from SPT-SZ and scales  $k'$  from *Planck* to measure  $\hat{\phi}(K = |k' - k|)$ . This is an important result showing that ongoing and future ground based experiments such as Simons Observatory or CMB-S4 will still benefit from combining the dataset from their large aperture telescopes with *Planck* to improve CMB lensing cluster mass measurements.

## 6. Modeling uncertainties

The errors quoted in the previous sections are only statistical. We investigated the impact of modeling uncertainties on our result in this Sect. 6. We studied the impact of the kSZ in Sect. 6.1. We considered the impact of the assumed cluster matter profile in the dedicated Sect. 6.2. We studied the effect of miscentering in Sect. 6.3. In Sect. 6.4 and 6.5, we studied the impact of the errors on cluster redshift and mass. Finally, we quantified the impact of

**Table 2.** Results on real maps changing the truncation radius used in the matched filter.

Truncation radius	$\frac{M_{\text{CMBlens}}}{M_{\text{SZ}}}$
$3 \times r_{500}$	$0.936 \pm 0.202$
$5 \times r_{500}$ (baseline)	$0.919 \pm 0.190$
$7 \times r_{500}$	$0.900 \pm 0.186$

the relativistic SZ effect in Sect. 6.6. Results are summarised in Table 5 and discussed in Sect. 6.7.

### 6.1. Impact of the kinetic SZ

The spectral energy distribution of the kSZ is similar to that of the CMB. Thus, we cannot separate those two components in the ILC and we want to check the impact the kSZ has on the final result.

We compare the results on simulated maps without kSZ, and with the kSZ signal induced by a normal velocity distribution of the galaxy clusters of 300 km/s, identical for all masses and redshifts. For each cluster, we performed 200 different draws of CMB, instrumental noise and velocity. We then had  $200 \times 468$  measurements that we compared with  $200 \times 468$  measurements with the same CMB and instrumental noise but a null velocity. On average over these 200 simulations, our result  $M_{\text{CMBlens}}/M_{\text{SZ}}$  was shifted by  $-0.060 \pm 0.015$ . The shift is the same for different CMB realizations, with a standard deviation (0.015) four times smaller than the shift (0.060). We decided to correct our final result accordingly. We note that Melin & Bartlett (2015) did not find a significant shift in their result due to the kSZ. This is because the shift is much smaller than the statistical error of their final result and they did not run enough simulations to extract the kSZ effect from the fluctuations of the statistical noise.

### 6.2. Impact of the assumed lensing profile in the matched filter

Our baseline analysis was performed with a matched filter, assuming a lensing profile based on a NFW profile truncated at  $5 \times r_{500}$ . The real lensing profile of individual clusters scatters around the NFW profile, but one also needs to consider that clusters are not isolated objects. They are located at the nodes of the cosmic web and are thus connected to filaments and sheets. Random structures may also be present on the line-of-sight. In order to assess the impact of our profile assumption on our result, we changed the truncation radius to a lower ( $3 \times r_{500}$ ) and a higher ( $7 \times r_{500}$ ) value. Our result  $M_{\text{CMBlens}}/M_{\text{SZ}}$  changed by  $+0.017$  and  $-0.019$  respectively (Table 2). The assumed profile thus had an impact on the result corresponding to about 10% of the statistical error bar. Separating the effects of filaments, sheets and random structures along the line-of-sight would require the use of N-body simulations, a work which is beyond the scope of this article.

### 6.3. Impact of the cluster miscentering

In our analysis, we used the cluster positions given by Bocquet et al. (2019). These positions are affected by an uncertainty. For this test, we used the simulated maps for which we know the exact positions of the clusters. We drew at random 468 "ob-

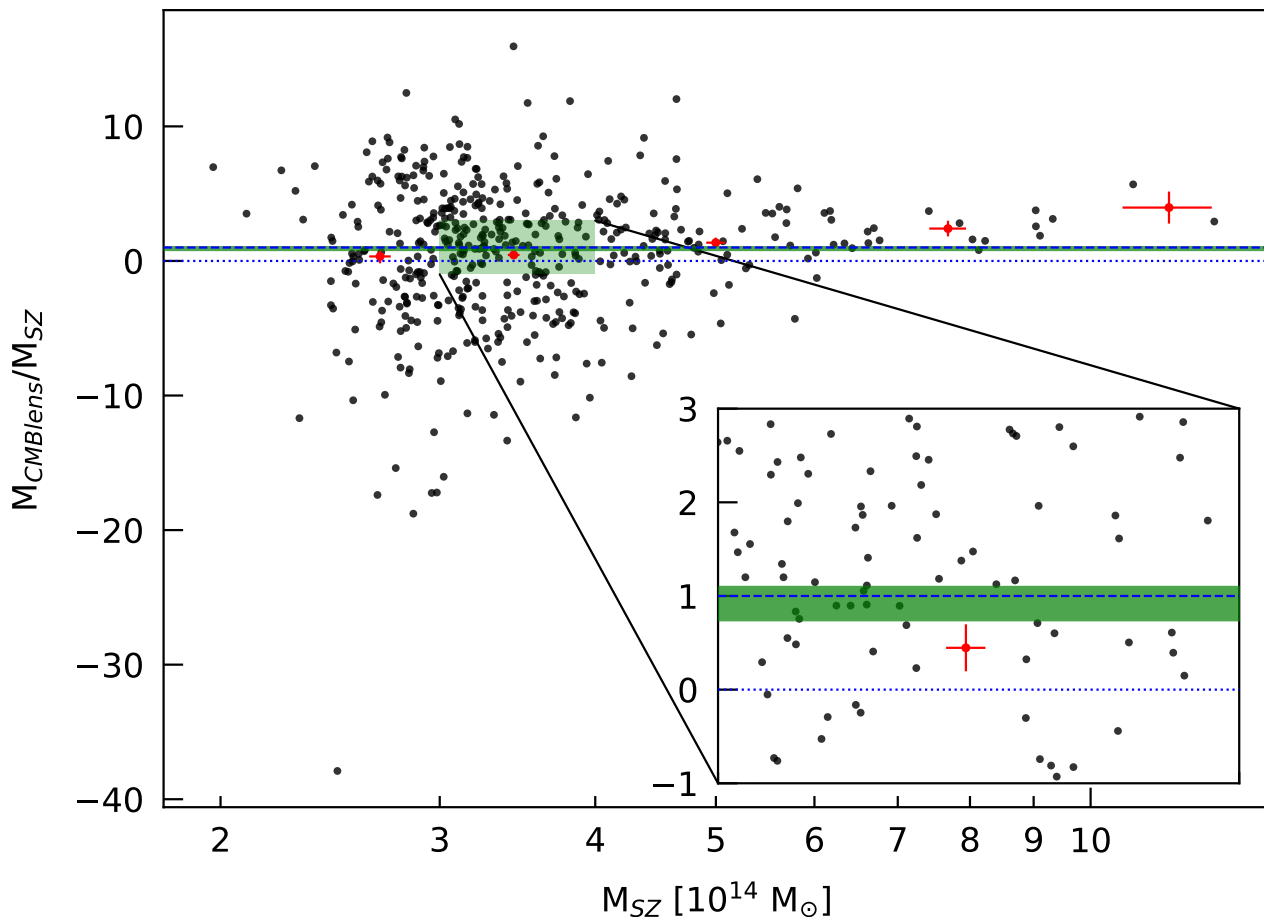


**Fig. 8.** Recovered CMB lensing mass  $M_{\text{CMBlens}}$  (divided by the SZ mass  $M_{\text{SZ}}$ ) as a function of SZ mass for the *Planck* + SPT-SZ combined analysis. Black dots are individual measurements. The red dots are the weighted means of the five mass bins, spaced logarithmically. The dotted (resp. dashed) blue line is the zero (resp. unity) level. The green stripe is the weighted mean within the error  $\langle M_{\text{CMBlens}}/M_{\text{SZ}} \rangle = 0.919 \pm 0.190$  (without correcting for the kSZ effect).

served" cluster positions from a normal law centered on the 468 "real" positions, with errors provided by Eq. 16 of [Melin & Pratt \(2023\)](#). We then performed the analysis on the maps, extracting the signal at the "real" and "observed" positions. The results are shown in Table 3. Without (resp. with) miscentering corresponds to signal extracted at "real" (resp. "observed") positions. We measured a bias  $\Delta \frac{M_{\text{CMBlens}}}{M_{\text{SZ}}} = +0.005$  much smaller than the error on the result  $\sigma = 0.181$ . We would need too many simulations to determine if the miscentering is only an increase in dispersion or if it also adds a systematic shift in the result.

An alternative method allowed us to obtain the same result without simulations: we used directly the lensing profile modeled for the matched filter and we computed the matched filter between a modeled profile at the "real" and at the "observed" positions. The error used in the matched filter computation is the one we get from the estimation of the lensing profile on real maps. We did this calculation 100 times (corresponding to 100 "observed" positions) for each of the 468 clusters. With this method, we find a shift of  $\Delta \frac{M_{\text{CMBlens}}}{M_{\text{SZ}}} = -0.008$ , close to the one obtained on simulated maps but much more precise. There is also a dispersion due to the velocity dispersion of the clusters of  $\Delta\sigma = 0.0005$  (calculated as the standard deviation across the 100

**Table 3.** Results on simulated maps with and without miscentering.

Miscentering	$\frac{M_{\text{CMBlens}}}{M_{\text{SZ}}}$
Without	$1.192 \pm 0.181$
With	$1.197 \pm 0.181$

"observed" positions), negligible with respect to the shift. With this, we show that miscentering creates a small negative bias in the result. We also used this alternative method to quantify the impact of the redshift and mass errors in the next sections.

#### 6.4. Impact of the redshift errors

Clusters are provided with their redshifts and associated errors. Once again, we performed the analysis on simulated maps for which we know the "real" redshifts. We drew "observed" redshifts with a normal law centered on the "real" ones with standard deviation given by the redshift uncertainty in the catalogue. The beginning of our analysis is not affected by a change in red-

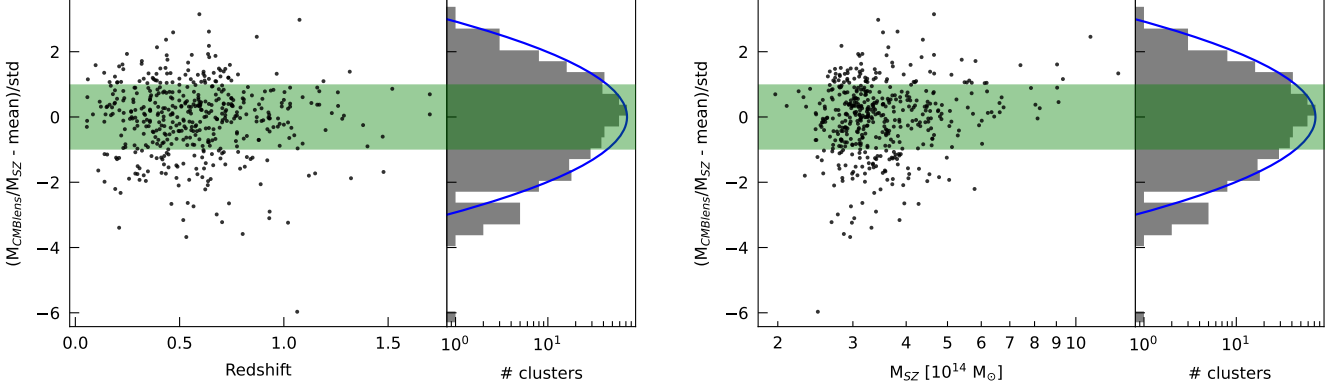


**Fig. 9.** Pull of the ratio  $M_{\text{CMBlens}}/M_{\text{SZ}}$  and associated histogram as a function of redshift (*Left*) and mass (*Right*). The blue line in each panel is a Gaussian centered on 0 with  $\sigma = 1$  for comparison.

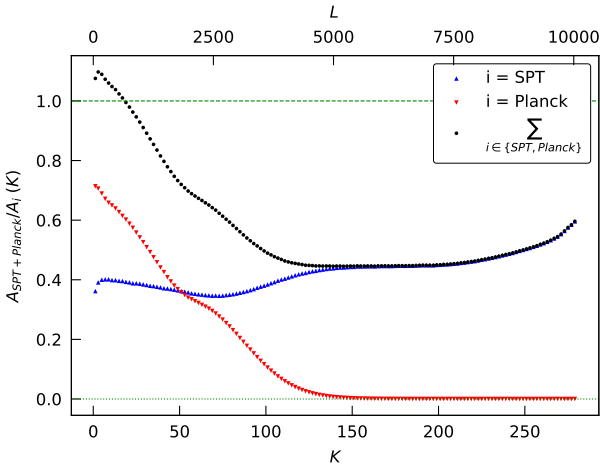


**Fig. 10.** Comparison of the variance  $A(K)$  of the lensing profile reconstructed for SPT-SZ and *Planck* binned in  $K = |k' - k|$  (or equivalently  $L = |l' - l|$ ). The figure displays the ratios between the combined  $A_{\text{SPT+Planck}}(K)$  and the single datasets  $A_i(K)$ , and the sum of both ratios. It shows that the *Planck* data set brings most of the information at large scales ( $K < 50.9$  or  $L < 1830$ ), while the SPT-SZ dataset provides information on the smaller scales ( $K > 145.0$  or  $L > 5208$ ). The sum is the product between the combined  $A_{\text{SPT+Planck}}$  term and the inverse variance sum  $1/A_{\text{SPT}} + 1/A_{\text{Planck}}$ . It is below unity for  $K > 18.9$  or  $L > 680$  demonstrating the significant gain of the combination with respect to individual measurements.

shift because no redshift information is used until the modeling of the lensing profile in the matched filter. Unfortunately, the change in the result due to the redshift uncertainty is too small to be measured with this method. We thus used the alternative method: we used the matched filter on a lensing profile modelled with the 100 "observed" 468-redshift sets, compared to one with the "real" redshifts. The impact of the redshift errors on the matched filter is a shift of  $\Delta \frac{M_{\text{CMBlens}}}{M_{\text{SZ}}} = +0.0002$  and a dispersion of about  $\Delta\sigma = 0.0008$ , which are negligible with respect to our statistical error  $\sigma = 0.190$ .

### 6.5. Impact of the error on the mass $M_{\text{SZ}}$

The direct method using simulations did not provide sufficient precision, as for the redshift. Once again, we used the alternative method, and applied the matched filter to compare the lensing profiles of the 468 clusters with "real" and "observed"  $M_{500}$ . We

**Table 4.** Results on real maps with and without the relativistic SZ effect.

Relativistic SZ effect	$\frac{M_{\text{CMBlens}}}{M_{\text{SZ}}}$
With	$0.919 \pm 0.190$
Without	$0.907 \pm 0.187$

used 40 draws. We obtained a mean bias of  $\Delta \frac{M_{\text{CMBlens}}}{M_{\text{SZ}}} = -0.0022$  and a dispersion of  $\Delta\sigma = 0.0070$ . Both are negligible with respect to the measured statistical error  $\sigma = 0.190$ .

### 6.6. Impact of the relativistic SZ effect

Our baseline result includes the relativistic SZ effect, that is  $j_{\nu_i}$  in Eq. 3 is computed including relativistic corrections to the SZ effect. Details of the implementation are provided in Sect. 4.2. We removed the relativistic correction from the calculation of  $j_{\nu_i}$  and re-ran the full analysis. We obtained a shift  $\Delta \frac{M_{\text{CMBlens}}}{M_{\text{SZ}}} = -0.012$ , of order of 10% of the statistical error bar. In Table 4, we compare our result on real data with and without including the relativistic SZ effect.

### 6.7. Summary of modeling uncertainties

Our modeling uncertainties are summarised in Table 5. The total error (errors added in quadrature) is 0.026 corresponding to about 14% of the statistical error (0.190). This demonstrates that the analyses based on the current data sets are dominated by statistical error driven by the instrumental noise of the experiments. Note that we did not include the relativistic SZ effect in our total error for the modeling uncertainties because it is a known effect which has to be included in the baseline analysis, and we only wanted to quantify its impact on our final results. This is the reason why it is included as a separate line at the bottom of the table. Similarly, we only added the dispersion due to kSZ in the total error as we correct for the kSZ bias in the final result.

## 7. Summary and conclusions

We performed the first CMB-lensing galaxy cluster mass measurement using a combination of ground and space-based surveys. We used the SPT-SZ cluster catalogue and extracted its average CMB lensing to SZ mass ratio from the SPT-SZ and

**Table 5.** Summary of the impact of the considered uncertainties on the measurement  $M_{\text{CMBlens}}/M_{\text{SZ}}$ . The major uncertainty is the profile modeling (about 10% of the statistical error). The other uncertainties are of order of 1%. The considered uncertainties and their modelings are described in dedicated subsections in Sect. 6.

Uncertainty	$\Delta \frac{M_{\text{CMBlens}}}{M_{\text{SZ}}}$
Dispersion due to kSZ	$\pm 0.015$
Profile up to $3 \times r_{500}$	$+0.017$
Profile up to $7 \times r_{500}$	$-0.019$
Miscentering	$-0.008$
Error on $z$	$\pm 0.001$
Error on $M_{500}$	$\pm 0.007$
<b>Total</b>	<b><math>\pm 0.026</math></b>
Bias due to kSZ	$-0.060$
No relativistic SZ	$-0.012$

*Planck* data sets. We found that the joint extraction outperforms the extraction on single datasets. This was not guaranteed a priori because SPT-SZ and *Planck* data observe the same primary CMB anisotropies, so the observations could have been fully correlated, and the combination unproductive. This is not the case. We detected the average CMB-lensing signal at  $4.8\sigma$  in the joint analysis compared with  $3.7\sigma$  for the *Planck* only and  $3.9\sigma$  for the SPT-SZ only analysis. We measured, before correcting for the kSZ,  $M_{\text{CMBlens}}/M_{\text{SZ}} = 0.92 \pm 0.19$  for the combination,  $M_{\text{CMBlens}}/M_{\text{SZ}} = 1.03 \pm 0.27$  for the *Planck* only analysis, and  $M_{\text{CMBlens}}/M_{\text{SZ}} = 1.12 \pm 0.29$  for the SPT-SZ only analysis. For the SPT-SZ only analysis, our measured mass ratio is in agreement with the mass ratio measured by Baxter et al. (2015) on a similar cluster sample and data set. Our final combined result, after correcting for the kSZ effect, is

$$M_{\text{CMBlens}}/M_{\text{SZ}} = 0.98 \pm 0.19 \text{ (stat.)} \pm 0.03 \text{ (syst.)}.$$

Our measurement is dominated by the statistical error. We estimated the modeling uncertainties to be of order of 14% of the statistical error.

We computed  $M_{\text{CMBlens}}/M_{\text{SZ}}$ , with  $M_{\text{SZ}} = 0.8 \times M_{\text{SPT}}$  where  $M_{\text{SPT}}$  is the mass given by Bocquet et al. (2019). This rescales the SPT masses to the level of *Planck* masses. This shift between *Planck* and SPT masses is recognized as a correction of a X-ray measurement (hydrostatic and instrumental) mass bias  $b$ , where the SPT analysis finds the bias to be  $b = 0.2$ . Since we "re-biased" the measurement, if  $M_{\text{SPT}}$  were an unbiased estimate of the CMB lensing mass, then our expected measurement should be  $M_{\text{CMBlens}}/M_{\text{SZ}} = M_{\text{CMBlens}}/(0.8 \times M_{\text{SPT}}) = 1.25$  instead of 1. Our measurement is compatible with both  $M_{\text{CMBlens}}/M_{\text{SZ}} = 1.25$  ( $b = 0.2$ ) and  $M_{\text{CMBlens}}/M_{\text{SZ}} = 1$  ( $b = 0$ ).

The analysis method is based on an internal linear combination of SPT-SZ and *Planck* maps that reconstructs the best primary CMB maps around clusters and nullifies the SZ effect. An optimal quadratic estimator is then applied to each CMB map to extract the cluster lensing potential. The last step consists in applying a matched filter to the lensing potential to measure the lensing mass and compare its value with the SZ mass. The analysis pipeline has been fully tested and characterized on simulations before being applied to the SPT-SZ and *Planck* data sets. The major technical difficulties of the analysis consist in taking properly into account the transfer function of the ground-based

experiment and dealing with the masking of point sources in the two data sets.

We showed that the gain from the ground and space-based combination with respect to analyses on individual data sets have two origins:

- The spatial scales observed by SPT-SZ and *Planck* do not fully overlap, so the two experiments bring different information from different primary CMB scales. *Planck* is more efficient at observing large scales while SPT-SZ is better at small scales.
- The cluster lens correlates scales. Our method allows to extract information from scales observed by *Planck* and scales observed by SPT-SZ that are correlated by the lens. This adds to the efficiency of the combination.

These results demonstrate that both small (of order of arcmin) and large (greater than 0.5 deg) scales are important for CMB-lensing cluster studies. CMB-lensing cluster mass measurements with upcoming and future ground-based large telescopes, such as Simons Observatory and CMB-S4, will therefore benefit from a combination with *Planck* to make full use of the lensing information.

*Acknowledgements.* We would like to thank Jim Bartlett, Jacques Delabrouille, Boris Bolliet, Íñigo Zubeldia and Erik Rosenberg for fruitful discussions about the results presented in this article. We are also grateful to members of the Cosmology group of the Particule Physics Department of CEA Paris-Saclay for useful discussions while progressing on this analysis. We would also like to thank Jim Rich for his helpful comments and suggestions on parts of this article. We acknowledge the use of the Legacy Archive for Microwave Background Data Analysis (LAMBDA), part of the High Energy Astrophysics Science Archive Center (HEASARC). HEASARC/LAMBDA is a service of the Astrophysics Science Division at the NASA Goddard Space Flight Center. We also acknowledge the use of the Planck Legacy Archive. We used the HEALPix software (Górski et al. 2005) available at <https://healpix.sourceforge.io> and the WebPlotDigitizer (Rohatgi 2022).

## References

- Abazajian, K., Addison, G., Adshead, P., et al. 2019, arXiv e-prints, arXiv:1907.04473
- Abbott, T. M. C., Aguena, M., Alarcon, A., et al. 2020, Phys. Rev. D, 102, 023509
- Ade, P., Aguirre, J., Ahmed, Z., et al. 2019, J. Cosmology Astropart. Phys., 2019, 056
- Albrecht, A., Bernstein, G., Cahn, R., et al. 2006, arXiv e-prints, astro
- Allen, S. W., Evrard, A. E., & Mantz, A. B. 2011, ARA&A, 49, 409
- Allen, S. W., Schmidt, R. W., & Fabian, A. C. 2002, MNRAS, 334, L11
- Arnaud, M., Pratt, G. W., Piffaretti, R., et al. 2010, Astronomy and Astrophysics, 517, A92, arXiv:0910.1234 [astro-ph]
- Bahcall, N. A., Fan, X., & Cen, R. 1997, ApJ, 485, L53
- Bartelmann, M. & Schneider, P. 2001, Physics Reports, 340, 291, arXiv:astro-ph/9912508
- Baxter, E. J., Keisler, R., Dodelson, S., et al. 2015, ApJ, 806, 247
- Baxter, E. J., Raghunathan, S., Crawford, T. M., et al. 2018, Monthly Notices of the Royal Astronomical Society, 476, 2674
- Benoit-Lévy, A., Déchelette, T., Benabed, K., et al. 2013, Astronomy & Astrophysics, 555, A37, arXiv:1301.4145 [astro-ph]
- Bleem, L. E., Stalder, B., de Haan, T., et al. 2015, The Astrophysical Journal Supplement Series, 216, 27, arXiv:1409.0850 [astro-ph]
- Bocquet, S., Dietrich, J. P., Schrabback, T., et al. 2019, The Astrophysical Journal, 878, 55, publisher: The American Astronomical Society
- Bulbul, E., Chiu, I. N., Mohr, J. J., et al. 2019, ApJ, 871, 50
- Carlberg, R. G., Yee, H. K. C., Ellingson, E., et al. 1996, ApJ, 462, 32
- Carlstrom, J. E., Holder, G. P., & Reese, E. D. 2002, Annual Review of Astronomy and Astrophysics, 40, 643, arXiv:astro-ph/0208192
- Chan, V. C., Hložek, R., Meyers, J., & van Engelen, A. 2023, arXiv e-prints, arXiv:2302.13350
- Chaubal, P. S., Reichardt, C. L., Gupta, N., et al. 2022, ApJ, 931, 139
- Chown, R., Omori, Y., Aylor, K., et al. 2018, The Astrophysical Journal Supplement Series, 239, 10, aDS Bibcode: 2018ApJS..239...10C
- Diemer, B. & Kravtsov, A. V. 2015, ApJ, 799, 108

- Dodelson, S. 2004, *Phys. Rev. D*, 70, 023009
- Geach, J. E. & Peacock, J. A. 2017, *Nature Astronomy*, 1, 795
- Geach, J. E., Peacock, J. A., Myers, A. D., et al. 2019, *ApJ*, 874, 85
- Górski, K. M., Hivon, E., Banday, A. J., et al. 2005, *ApJ*, 622, 759
- Gupta, N. & Reichardt, C. L. 2021, *ApJ*, 923, 96
- Hasselfield, M., Hilton, M., Marriage, T. A., et al. 2013, *J. Cosmology Astropart. Phys.*, 2013, 008
- Hoffman, Y. & Ribak, E. 1991, *The Astrophysical Journal*, 380, L5, aDS Bibcode: 1991ApJ...380L...5H
- Holder, G. & Kosowsky, A. 2004, *ApJ*, 616, 8
- Horowitz, B., Ferraro, S., & Sherwin, B. D. 2019, *MNRAS*, 485, 3919
- Hu, W., DeDeo, S., & Vale, C. 2007, *New Journal of Physics*, 9, 441
- Hu, W. & Okamoto, T. 2002, *The Astrophysical Journal*, 574, 566, arXiv:astro-ph/0111606
- Itoh, N., Kohyama, Y., & Nozawa, S. 1998, *ApJ*, 502, 7
- Laureijs, R., Amiaux, J., Arduini, S., et al. 2011, arXiv e-prints, arXiv:1110.3193
- Levy, K., Raghunathan, S., & Basu, K. 2023, arXiv e-prints, arXiv:2305.06326
- Lewis, A. & Challinor, A. 2006, *Phys. Rep.*, 429, 1
- Lewis, A. & King, L. 2006, *Phys. Rev. D*, 73, 063006
- Louis, T. & Alonso, D. 2017, *Phys. Rev. D*, 95, 043517
- LSST Science Collaboration, Abell, P. A., Allison, J., et al. 2009, arXiv e-prints, arXiv:0912.0201
- Ludlow, A. D., Bose, S., Angulo, R. E., et al. 2016, *MNRAS*, 460, 1214
- Madhavacheril, M., Sehgal, N., Allison, R., et al. 2015, *Phys. Rev. Lett.*, 114, 151302
- Madhavacheril, M. S., Battaglia, N., & Miyatake, H. 2017, *Phys. Rev. D*, 96, 103525
- Madhavacheril, M. S. & Hill, J. C. 2018, *Phys. Rev. D*, 98, 023534
- Madhavacheril, M. S., Sifón, C., Battaglia, N., et al. 2020, *ApJ*, 903, L13
- Maturi, M., Bartelmann, M., Meneghetti, M., & Moscardini, L. 2005, *A&A*, 436, 37
- Melin, J.-B. & Bartlett, J. G. 2015, *Astronomy & Astrophysics*, 578, A21, arXiv:1408.5633 [astro-ph]
- Melin, J. B., Bartlett, J. G., Tarrío, P., & Pratt, G. W. 2021, *A&A*, 647, A106
- Melin, J. B. & Pratt, G. W. 2023, *A&A*, 678, A197
- Nagai, D., Kravtsov, A. V., & Vikhlinin, A. 2007, *The Astrophysical Journal*, 668, 1, arXiv:astro-ph/0703661
- Navarro, J. F., Frenk, C. S., & White, S. D. M. 1996, *The Astrophysical Journal*, 462, 563, arXiv:astro-ph/9508025
- Patil, S., Raghunathan, S., & Reichardt, C. L. 2020, *ApJ*, 888, 9
- Planck Collaboration, Ade, P. A. R., Aghanim, N., et al. 2016a, *A&A*, 594, A27
- Planck Collaboration, Ade, P. A. R., Aghanim, N., et al. 2016b, *A&A*, 594, A13
- Planck Collaboration, Ade, P. A. R., Aghanim, N., et al. 2016c, *A&A*, 594, A24
- Planck Collaboration, Aghanim, N., Akrami, Y., et al. 2020a, *A&A*, 641, A1
- Planck Collaboration, Aghanim, N., Akrami, Y., et al. 2020b, *A&A*, 641, A1
- Raghunathan, S., Bianchini, F., & Reichardt, C. L. 2018, *Phys. Rev. D*, 98, 043506
- Raghunathan, S., Holder, G. P., Bartlett, J. G., et al. 2019a, *J. Cosmology Astropart. Phys.*, 2019, 037
- Raghunathan, S., Patil, S., Baxter, E., et al. 2019b, *ApJ*, 872, 170
- Raghunathan, S., Patil, S., Baxter, E., et al. 2019, *Phys. Rev. Lett.*, 123, 181301
- Raghunathan, S., Patil, S., Baxter, E. J., et al. 2017, *J. Cosmology Astropart. Phys.*, 2017, 030
- Raghunathan, S., Whitehorn, N., Alvarez, M. A., et al. 2022, *ApJ*, 926, 172
- Remazeilles, M., Delabrouille, J., & Cardoso, J.-F. 2011, *Monthly Notices of the Royal Astronomical Society*, 410, 2481, arXiv:1006.5599 [astro-ph]
- Rohatgi, A. 2022, *Webplotdigitizer: Version 4.6*
- Ruhl, J., Ade, P. A. R., Carlstrom, J. E., et al. 2004, in *Society of Photo-Optical Instrumentation Engineers (SPIE) Conference Series*, Vol. 5498, Z-Spec: a broadband millimeter-wave grating spectrometer: design, construction, and first cryogenic measurements, ed. C. M. Bradford, P. A. R. Ade, J. E. Aguirre, J. J. Bock, M. Dragovan, L. Duband, L. Earle, J. Glenn, H. Matsuhara, B. J. Naylor, H. T. Nguyen, M. Yun, & J. Zmuidzinas, 11–29
- Seljak, U. & Zaldarriaga, M. 2000, *ApJ*, 538, 57
- Story, K. T., Reichardt, C. L., Hou, Z., et al. 2013, *ApJ*, 779, 86
- Swetz, D. S., Ade, P. A. R., Amiri, M., et al. 2011, *ApJS*, 194, 41
- Tarrío, P., Melin, J. B., & Arnaud, M. 2019, *A&A*, 626, A7
- Vale, C., Amblard, A., & White, M. 2004, *New A*, 10, 1
- Vikhlinin, A., Kravtsov, A. V., Burenin, R. A., et al. 2009, *ApJ*, 692, 1060
- White, S. D. M., Navarro, J. F., Evrard, A. E., & Frenk, C. S. 1993, *Nature*, 366, 429
- Yoo, J. & Zaldarriaga, M. 2008, *Phys. Rev. D*, 78, 083002
- Yoo, J., Zaldarriaga, M., & Hernquist, L. 2010, *Phys. Rev. D*, 81, 123006
- Zaldarriaga, M. & Seljak, U. 1999, *Phys. Rev. D*, 59, 123507
- Zubeldia, Í. & Challinor, A. 2019, *MNRAS*, 489, 401
- Zubeldia, Í. & Challinor, A. 2020, *MNRAS*, 497, 5326